Morphology and Orientational Behavior of Silica-Coated Spindle-Type Hematite Particles in a Magnetic Field Probed by Small-Angle X-ray Scattering

Mathias Reufer,[†] Hervé Dietsch,[†] Urs Gasser,[‡] Ann Hirt,[§] Andreas Menzel,[||] and Peter Schurtenberger*,[†]

Adolphe Merkle Institute and Fribourg Center for Nanomaterials, University of Fribourg, 1723 Marly, Switzerland, Laboratory for Neutron Scattering, ETH Zürich & Paul Scherrer Institut, 5232 Villigen PSI, Switzerland, Institute for Geophysics, ETH Zürich, Switzerland, and Swiss Light Source, Paul Scherrer Institut, 5232 Villigen PSI, Switzerland

Form factor and magnetic properties of silica-coated spindle-type hematite nanoparticles are determined from SAXS measurements with applied magnetic field and magnetometry measurements. The particle size, polydispersity and porosity are determined using a core−shell model for the form factor. The particles are found to align with their long axis perpendicular to the applied field. The orientational order is determined from the SAXS data and compared to the orientational order obtained from magnetometry. The direct access to both, the orientational order of the particles, and the magnetic moments allow one to determine the magnetic properties of the individual spindle-type hematite particles. We study the influence of the silica coating on the magnetic properties and find a fundamentally different behavior of silica-coated particles. The silica coating reduces the effective magnetic moment of the particles. This effect is enhanced with field strength and can be explained by superparamagnetic relaxation in the highly porous particles.

Introduction

The distinct magnetic properties of colloidal particles are receiving considerable attention not only in the traditional field of data storage applications, but more recently for protein and cell separation techniques,[1,2] medical applications in oncology, or as magnetic contrast agents.[3] For these applications, detailed knowledge of the particle morphology, size, and of the magnetic response to an applied magnetic field is essential. Generally, morphological characterization is extracted from transmission electron microscopy (TEM) images, which can be ambiguous due to aggregation or collapse of the particle on the TEM grid during drying and, moreover, only gives limited statistics. In addition, the internal structure of particles such as a core−shell structure or pores, which are especially relevant in medical applications for encapsulation and biocompatibility, are often difficult to resolve.

Scattering experiments allow characterization over length scales covering particle dimensions down to the internal structure[4] and shell structures can be resolved by using core−shell form factors.[5] Moreover, scattering experiments provide information on the orientational order of dispersed anisotropic particles. This information is crucial to study model systems of colloidal particles with anisotropic interaction potential.[6] Furthermore, the orientational order of magnetic particles in a magnetic field is associated with the magnetic properties of the particles. Magnetic properties of nanosized or highly porous particles are often governed by surface effects and are sensitive to stress[7] and therefore, may depend on sample preparation. Scattering experiments allow in situ measurements of dispersed particles and therefore exclude artifacts due to sample preparation that can be problematic for conventional magnetometry.

In our study we investigate porous spindle-type hematite particles with silica coating. Hematite (α-Fe_2O_3) is the most stable phase of iron oxide in air at ambient conditions. Hematite spindle-type particles can be synthesized at a gram scale at moderate polydispersity with different aspect ratios and sizes depending on the synthesis method and conditions.[8−10] A silica coating is of particular interest for biocompatibility, for enhanced colloidal stability at neutral pH, and to control the surface chemistry via silane chemistry.[10,11]

Scattering experiments on hematite particles are conventionally done using X-rays due to the high absorption in the visible spectrum. For anisotropic particles, the obtained anisotropic two-dimensional (2D) scattering patterns can be linked directly to the orientation of the dispersed particles, which can be described by an orientational order parameter. The small magnetic moments and the low concentrations (<1 wt %) of the investigated particles allow one to assume that excluded volume and magnetic dipole interactions are negligible compared to the interactions of the magnetic moment with the applied external magnetic field. Thus, the individual particles diffuse freely, and an applied homogeneous magnetic field only aligns the particles. We therefore describe the resulting scattering pattern of dispersed silica-coated spindle-type hematite particles with the form factor of a core−shell ellipsoid,[5,12] in which we have added randomly distributed pores to take the porous hematite core into account.

Synthesis and Experimental Methods

We study spindle type hematite particles labeled as F0, synthesized by the previously reported method developed by Ocaña and co-workers.[9] In addition, part of the F0-particles are coated with a silica layer[11,10] and are labeled F1 to F3.

* To whom correspondence should be addressed: E-mail: peter.schurtenberger@unifr.ch.
[†] University of Fribourg.
[‡] Laboratory for Neutron Scattering, ETH Zürich & Paul Scherrer Institut.
[§] Institute for Geophysics, ETH Zürich.
[||] Swiss Light Source, Paul Scherrer Institut.

TABLE 1: Fit Parameters for Isotropically Oriented Particles from Scattering Experiments[a] and Fit Parameters for Magnetization Curve of Dispersed Particles[b]

	$\bar{a}$ [nm]	$\bar{b}$ [nm]	p_b [%]	$\bar{s}$ [nm]	p_s [%]	N_{p1}	ρ_{shell} [nm^{-2}]	M_{sat} [(Am^2)/(kg)]	μ [(J)/(T)]	χ_m [(Am^4)/(Vskg)]
Δ	±5	±0.3		±0.3			$\pm 0.05 \times 10^{-3}$	±0.04	$\pm 0.3 \times 10^{-19}$	±0.02
F0	117	18.6	22	0.00	0.0	180		0.42	1.6×10^{-19}	0.30
F1	132	31.5	24	13.3	22	120	1.58×10^{-3}			
F2	148	47.8	13	29.9	10	900	1.59×10^{-3}	0.28	2.8×10^{-19}	0.12
F3	173	75.3	13	57.5	7.0	1200	1.68×10^{-3}			

[a] Mean particle semi-axes $\bar{a}$ and $\bar{b}$, polydispersity in b: p_b, mean shell thickness $\bar{s}$, and associated polydispersity p_s, number of pores N_{p1}, scattering length density of the shell ρ_{shell}. [b] Saturation magnetization M_{sat}, magnetic moment μ of a single particle, susceptibility χ_m. The Δ-line contains the absolute errors.

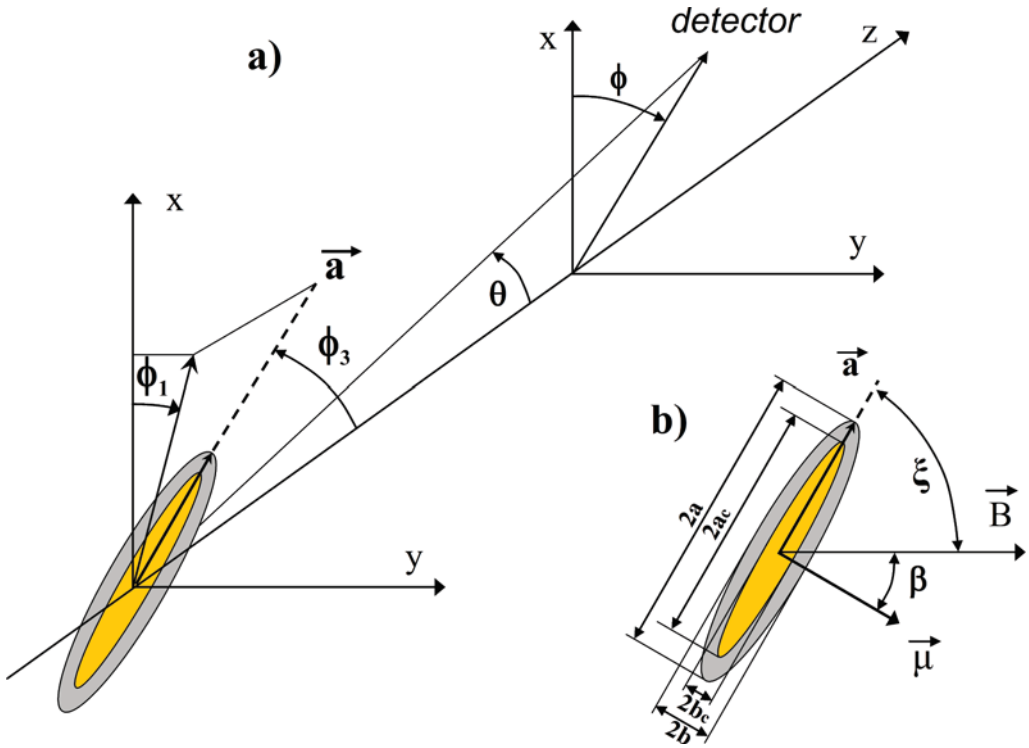

Figure 1. (a) Schematic showing the scattering geometry used. (b) A core−shell particle with major semiaxis a in a magnetic field B with the definition of the angles to calculate E_{pot}.

Iron(III) perchlorate hexahydrate $Fe(ClO_4)_3 \cdot 6H_2O$, polyvinylpyrrolidone (PVP, 10000 g/mol) and 25 wt % tetramethylammonium hydroxide (TMAH) solution in water were purchased from Sigma Aldrich and used as received. Sodium dihydrogen phosphate monohydrate ($NaH_2PO_4 \cdot H_2O$), urea, and absolute ethanol from Fluka and tetraethyl orthosilicate (TEOS) from Merck were also used without further purification. Ultra pure water (resistivity = 18.2 MΩ·cm) purified by a Milli-Q system was used throughout the experiments.

One hundred fifty-six grams of $Fe(ClO_4)_3 \cdot 6H_2O$, 1.88 g of H_2NaPO_4, and 15.1 g of urea were dispersed in 2.5 L of Milli-Q water and aged for 24 h at 98 °C in an oven. The particles are obtained as a brownish sediment, which can be concentrated and cleaned by centrifuging and redispersing in water. We refer to the resulting particles as F0. For a typical 13 nm thick silica coating, 250 mg of F0 particles was dispersed in 100 mL of Milli-Q water, 2.0 g of PVP was then added to the solution, and it was stirred overnight. The excess of the PVP was removed by centrifuging, and the PVP-stabilized hematite particles were dispersed in a mixture of 10 mL of water and 225 mL of ethanol and were stirred mechanically at 400 rpm in a plastic bottle. Three hundred milligrams of TMAH (25 wt %) was then added, and 2.9 mL of TEOS was diluted by 3 mL ethanol and added in four portions to the stirred suspension every 30 min. The stirring was continued for 8 more hours, after which the F1 particles were washed with water. Particles denoted as F2 (F3) were obtained by coating particles of F1 (F2) again with silica following the same process. All the obtained samples F0−F3 were then stored in a mixture of water and 0.05 wt % TMAH. The TMAH sets the pH to ∼10 and increases the stability by charging the particles negatively.[13] The weight concentrations of samples F0−F3 were 0.2, 0.5, 1.0, and 0.8%, respectively, and were determined by drying at 70 °C and weighing a small fraction of the batch.

TEM was performed on a Philips CM100-Biotwin at 80 keV and on a CM200 operated at 200 keV. For the sample preparation, a droplet of particles dispersed in ethanol was dried onto a carbon-coated copper grid. The mean particle dimensions were determined from a statistical analysis of TEM images; approximately 200 particle contours are fitted with ellipses corresponding to prolate spheroids of a given cross section. Small-angle X-ray scattering (SAXS) was performed at the cSAXS beamline at 11.2 keV (corresponding to a wavelength of λ = 0.111 nm) at the Swiss Light Source (Paul Scherrer Institute, Villigen, Switzerland). The magnetic field was applied using a water-cooled electromagnet (Buckley Systems, Ltd.) that was tilted by an angle 10° relative to the horizontal direction to avoid contributions of slit scattering along the field direction.

The dispersed particles were measured in 1.0 mm quartz capillaries at 24 °C. The solvent was measured separately and subtracted from the data. For each sample, 20 measurements were performed: 12 measurements with increasing magnetic field, and 8 subsequent measurements with decreasing field. Because of the remanent moment of the iron cores of the electromagnet, a residual flux density of 6.6 mT was found at zero current. For a more detailed analysis of the internal structure of the F0 sample, this sample was measured with a pinhole wide-angle X-ray scattering (WAXS) camera from Rigaku Innovative Technologies equipped with a microfocus X-ray source. Magnetization curves of dispersed particles (sealed plastic containers of 100 μL volume) were measured using a vibrating sample magnetometer (PMC model 3900). To take the effective mass content of hematite into account, the magnetization data of sample F2 was corrected by the hematite mass fraction $m_{hem}/m_{part} = 0.18$, which is calculated based on the densities[14] of $d_{hem} = 5.26$ g/cm^3 and $d_{silica} = 2.06$ g/cm^3, the particle dimensions in Table 1, and a pore volume fraction of $v_p = 0.26$ of the hematite core by assuming that the pores are filled with silica. For the form factor model, a coordinate system with a magnetic field parallel to the y-axis was used, as shown in Figure 1a.

Form Factor of Porous Core−Shell Spindle-Type Particles

Beacuse of the low particle concentrations (≤1 wt %), we assume no positional correlation of the individual particles and describe the scattering intensity with the form factor of a core−shell ellipsoid,[5,12] where a_c, b_c and a, b are the semiaxes of the core and the total particle, respectively (see Figure 1b). In the absence of an applied magnetic field, the dispersed particles are randomly oriented, and the resulting 2D scattering pattern is isotropic, thus the scattering intensity does not depend on the angle ϕ in the detector plane shown in Figure 1a. With an applied magnetic field, the individual particles align, and the resulting 2D scattering pattern reflects the anisotropy of the particle shape. The equilibrium states are described by the Boltzmann factor $p(E_{pot})$, where the potential energy E_{pot} of a particle depends on the particle orientation given by ϕ_1 and ϕ_3 as depicted in Figure 1b. The scattering intensity is given by

$$I(q,\phi) = \sum_{j,k} f_j g_k P(q,\phi, vb_j, b_j, vb_j - s_k, b_j - s_k) \quad (1)$$

with the form factor

$$P(q,\phi,a,b,a_c,b_c) = \frac{1}{Z}\int_0^{2\pi}\int_0^{\pi} p(E_{pot})\{[\tilde{\rho}R(a,b) + \tilde{\rho}_c R(a_c,b_c)]^2 + \sum_m N_{pm}[\tilde{\rho}_p R(a_{pm},b_{pm})]^2\}\sin(\phi_3)d\phi_1 d\phi_3 \quad (2)$$

and

$$\begin{aligned}
Z &= \int_0^{2\pi}\int_0^{\pi} p(E_{pot})\sin(\phi_3)d\phi_1 d\phi_3\\
R(a,b) &= \frac{3}{u^3(a,b)}[\sin(u(a,b)) - u(a,b)\cos(u(a,b))]\\
u(a,b) &= q\sqrt{(a^2-b^2)x^2 + b^2}\\
x &= \cos(\phi_3)\cos(\gamma) + \sin(\phi_3)\sin(\gamma)\cos(\phi_1 - \phi)\\
\gamma &= a\sin\left(\frac{\lambda q}{4\pi}\right) + \frac{\pi}{2}\\
v_p &= \sum_m N_{pm} V(a_{pm},b_{pm})/V(\bar{a},\bar{b})\\
\rho_c &= (1-v_p)\rho_{hem} + v_p\rho_{water}\\
\tilde{\rho} &= V(a,b)(\rho_{shell} - \rho_{water})/r_e\\
\tilde{\rho}_c &= V(a_c,b_c)(\rho_c - \rho_{shell})/r_e\\
\tilde{\rho}_p &= V(a_p,b_p)(\rho_{water} - \rho_{hem})/r_e\\
V(a,b) &= \frac{4}{3}\pi a b^2
\end{aligned}$$

where $q = (4\pi/\lambda)\sin(\theta/2)$ is the absolute value of the scattering vector, and $r_e = 2.82 \times 10^{-15}$ m is the classical radius of the electron. The discrete probability density distributions f_j and g_k represent the polydispersity of b and s, respectively. Since the polydispersity of the aspect ratio $v = a/b$ is much smaller than that of b, we assume a constant aspect ratio and calculate the corresponding values for a directly from b. The polydispersity in the shell thickness s is taken into account by a discrete set of 5 log-normal-distributed values with mean value $\bar{s}$, polydispersity p_s and the probability density function g_k. The last term in eq 2 models the presence of randomly distributed pores in the hematite cores. We use a distribution where each pore size is represented by N_{pm} pores with semiaxes a_{pm} and b_{pm}, where $\vec{a}_{pm}$ is collinear with $\vec{a}$. The existence of pores is confirmed by TEM images (see inset of Figure 2) and is in agreement with observations made on similar particles.[15−17] The porosity reduces the effective scattering length density ρ_c. The values for the scattering length densities $\rho_{water} = 0.946 \times 10^{-3}$ nm^{-2} and $\rho_{hem} = 4.16 \times 10^{-3}$ nm^{-2} were calculated based on the densities $d_{water} = 1.0$ g/cm^3 and $d_{hem} = 5.26$ g/cm^3 and were used as fixed parameters. The scattering length density for the shell ρ_{shell} is treated as fitting parameter.

We use the Boltzmann factor $p(E_{pot}) = \exp(-(E_{pot})/(k_B T))$ where the potential energy of the particle is compared with the thermal energy $k_B T$. Assuming a constant magnetic moment μ in a homogeneous magnetic field with flux density B, we find the potential energy $E_{pot}(\beta) = -\mu B\cos(\beta)$, where β is the angle between $\vec{\mu}$ and $\vec{B}$ as sketched in Figure 1b. To link the orientation of $\vec{\mu}$ to the particle orientation $\vec{a}$, we need to consider the magnetic properties of hematite. Hematite has a corundum-type crystal structure with space group $R3\bar{c}$ and at room temperature is a canted antiferromagnet with a small resulting magnetic moment $\vec{\mu}$ in the basal plane (perpendicular to the c-axis).[18] The magnetic moment can switch rather easily in the basal plane due to the small magnetic anisotropy energy within the plane compared to the energy required to tilt $\vec{\mu}$ out of the basal plane.[18] It has been shown[16] that the synthesized spindle-type hematite particles are monocrystalline with the c-axis collinear to the major particle axis $\vec{a}$, and $\vec{\mu}$ is perpendicular to $\vec{a}$. Thus, in a magnetic field $\vec{B}$, the particle orientation $\vec{a}$ is only restricted to the plane perpendicular to $\vec{B}$, and the particles are free to rotate around the direction of $\vec{B}$ without increasing E_{pot}. We assume that, for a given particle orientation $\vec{a}$, the magnetic moment $\vec{\mu}$ orients in the basal plane such that the angle β and thus $E_{pot}(\beta)$ is minimal. This implies $0 \le \beta \le \pi/2$, and the process of minimizing β for a given particle position might be governed

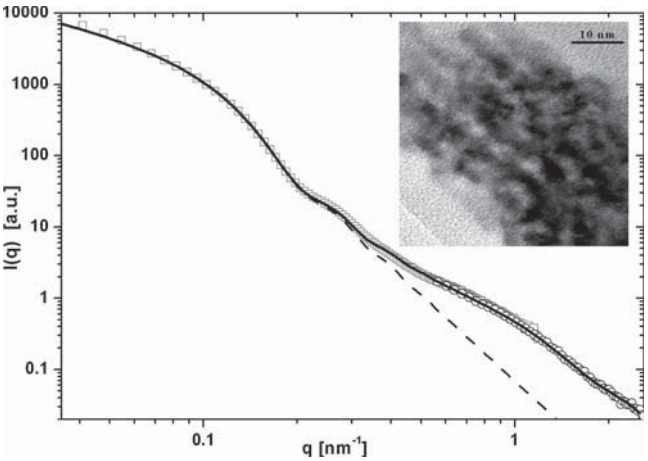

Figure 2. SAXS data (squares) and WAXS data (circles) of isotropically oriented particles F0. The solid line represents the calculation based on the parameters taken from Table 1 and the bimodal distribution of pores described in the text. Without taking pores into account, the calculated scattering curve reveals Porod behavior at high q values (dashed line). The inset shows a TEM image of an F0 particle where the strong contrast variations reflect the porous character of the hematite particles.

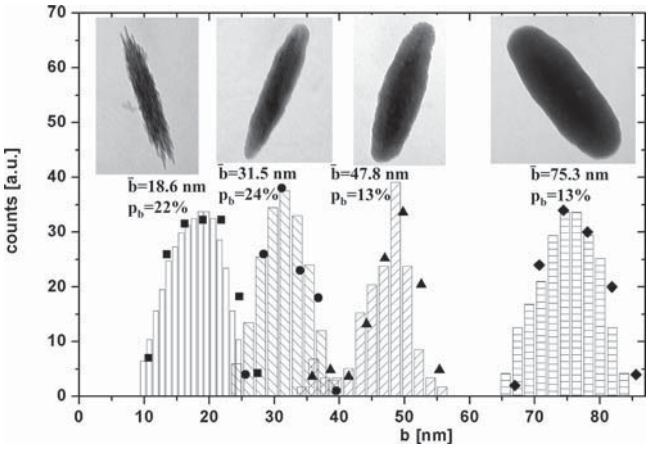

Figure 3. The distribution of the minor axis b found by particle sizing based on TEM images (F0 squares, F1 circles, F2 triangles, F3 diamonds), in good agreement with the probability density functions f_j (histograms) found from fitting the scattering curves. The mean $\bar{b}$ and polydispersity p_b are obtained from a Gauss-fit to the histograms. The TEM images show typical examples of the corresponding particles.

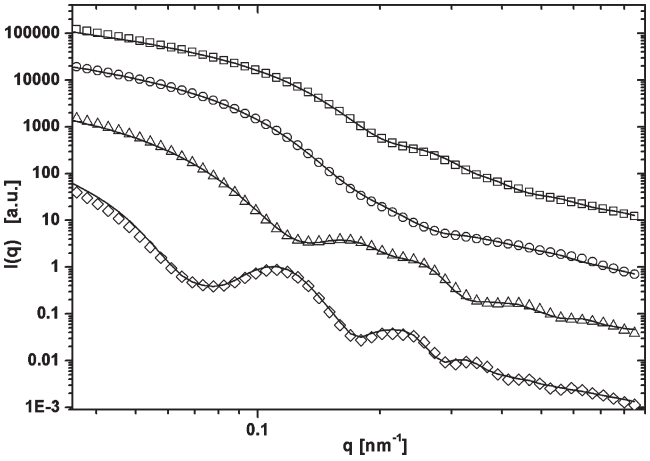

Figure 4. Scattering intensities of isotropically oriented particles F0 (squares), F1 (circles), F2 (triangles). and F3 (diamonds). The lines show calculations based on the parameters in Table 1. The curves are vertically shifted for clarity.

by particle rotation around $\vec{a}$ or by rotation of $\vec{\mu}$ in the basal plane of the crystal lattice. Thus

$$p(E_{\text{pot}}) = \exp\left(-\frac{E_{\text{pot}}(\beta)}{k_{\text{B}}T}\right) = \exp(\varepsilon \cos(\beta)) \qquad (3)$$

with $\varepsilon = \mu B/k_{\text{B}}T$. With the field direction $\vec{B}/B = (0, 1, 0)$ and the major axis direction $\vec{a}/a = (\sin(\phi_3)\ \cos(\phi_1), \sin(\phi_1)\ \sin(\phi_3), \cos(\phi_3))$ we find $\cos(\beta) = |(\vec{a}/a) \times (\vec{B}/B)| = (1 - \sin(\phi_1)^2\ \sin(\phi_3)^2)^{1/2}$.

Results and Discussion

In a first step we investigate the isotropically oriented samples, i.e., without applied magnetic field. The scattering curves are obtained by averaging the isotropic 2D scattering patterns over $0 \le \phi < 2\pi$ as depicted in Figure 1a. We first fit sample F0 where we have no shell and less fitting parameters. We measured this sample on a pinhole WAXS camera to extend the q-range to larger values, which allows for the determination of a quantitative value for the porosity in the hematite core. Figure 2 shows the data and the fit obtained using eq 1 with $p(E_{\text{pot}}) = 1$ and the parameters listed in Table 1. The best fit is found when taking a bimodal distribution of $N_{\text{p1}} = 180$ elliptical pores with a major semiaxis of $a_{\text{p1}} = 5.7$ nm and a minor semiaxis of $b_{\text{p1}} = 2.2$ nm and $N_{\text{p2}} = 3200$ spherical pores of $a_{\text{p2}} = b_{\text{p2}} = 1.2$ nm radius. The larger pores can be associated with those visible in the TEM image in the inset of Figure 2 and lead to the broad feature at $q = 1$ nm^{-1} in Figure 2. The small pores of 1.2 nm radius give rise to the small hump at $q = 2$ nm^{-1} and might represent surface roughness. The sum of both contributions yields a total pore volume fraction of $v_{\text{p}} = 0.26$.

For the fits of the SAXS data of the silica-coated particles F1−F3, we fix the pore sizes, N_{p2}, and $v_{\text{p}} = 0.26$ that were determined from the fit of F0. N_{p1} is, therefore, the only fit parameter for the pores, since the restricted q-range does not allow one to distinguish different pore sizes. To take particle size polydispersity into account, discrete distributions f_j are used for the minor semiaxes b as shown in Figure 3. A Gauss-fit determines the mean values $\bar{b}$ and polydispersity p_b. Figure 4 shows the scattering data and the corresponding calculated curves obtained with the best-fit parameters listed in Table 1. The shell thickness s increases for samples F0−F3, and the polydispersity p_s decreases (Table 1), as expected. A large silica layer yields more Stöber-like particles, which are known to have a smaller polydispersity compared to uncoated hematite particles. Taking polydispersity into account, the particle and shell sizes of F1, F2, and F3 agree very well with the core size found from F0.

The number of pores N_{p1} is considerably lower for F1 compared to F0. This can be explained by silica-filled pores in the hematite core, which have a decreased scattering contrast compared to pores filled with water. However, the assumption that pores in the hematite core are filled with silica is supported by the observation that the values found for the shell scattering length densities $\rho_{\text{shell}} = 1.58 \times 10^{-3}$ nm^{-2} to 1.68×10^{-3} nm^{-2} are all smaller than expected for Stöber-like silica (1.78×10^{-3} nm^{-2} for a density $d_{\text{silica}} = 2.06$ g/cm^3).[14] The model given by eq 1 assumes water-filled pores and thus underestimates ρ_{c}. Since the fit is sensitive only to the relative scattering contrast, ρ_{shell} is also underestimated. When adapting the model to pores filled with silica (by replacing ρ_{water} with ρ_{shell} to calculate $\tilde{\rho}_{\text{p}}$

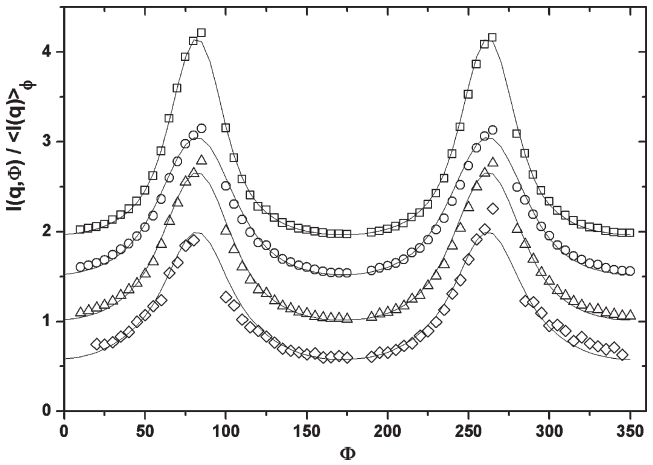

Figure 5. Angular dependency of the scattering intensities of F0 (squares), F1 (circles), F2 (triangles), and F3 (diamonds) at $q = 0.081$ nm^{-1} (0.053 nm^{-1} for F3) for an applied field of $B = 1.0$ T. The lines are the calculations based on the parameters in 1 and the best-fit values for $\bar{\varepsilon}$. The data sets are vertically shifted for clarity by 0.5 from each other.

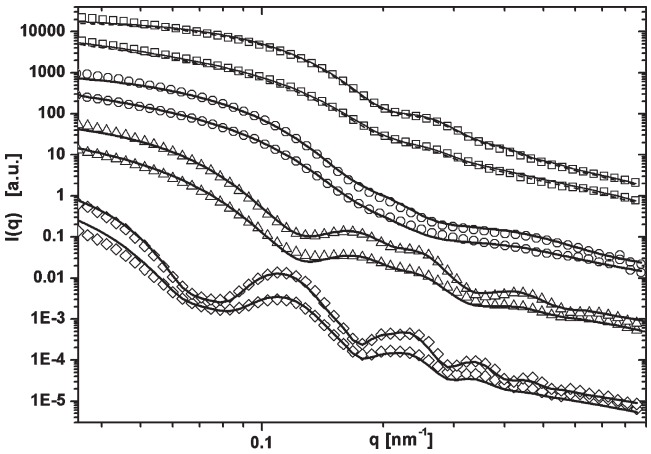

Figure 6. Scattering intensities of F0 (squares), F1 (circles), F2 (triangles), and F3 (diamonds) in scattering direction parallel (upper curve) and perpendicular (lower curve) for an applied field of $B = 1.0$ T. The data sets are vertically shifted for clarity. The lines are the calculations based on the parameters in Table 1 and the best-fit values for $\bar{\varepsilon}$.

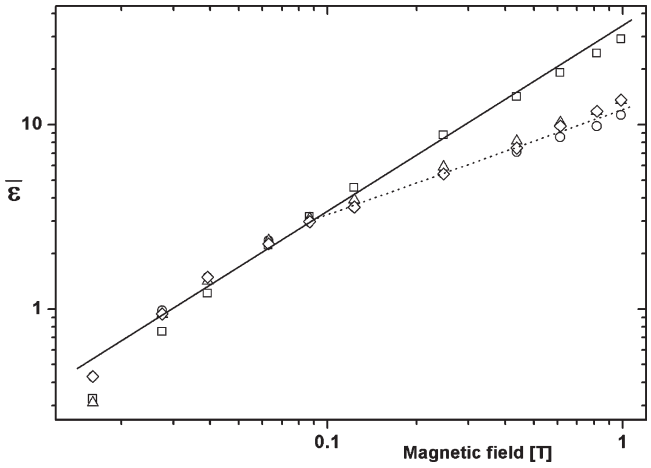

Figure 7. Energy parameters $\bar{\varepsilon}$ obtained from fits of the scattering curves. For F0 (squares) a linear scaling is found (solid line has a slope of 1), whereas, for the silica-coated samples F1 (circles), F2 (triangles), and F3 (diamonds), a distinct deviation around 100 mT is observed (dotted line is a guideline for the eyes).

and ρ_c in eq 2) we find ρ_{shell} in the range from 1.63×10^{-3} nm^{-2} to 1.73×10^{-3} nm^{-2} corresponding to silica densities from $d_{silica} = 1.90$ g/ cm^3 to 2.02 g/cm^3. These values are still less than values given in the literature for Stöber-like silica, which reflects a high porosity inside the silica shell. A highly porous shell is also confirmed by the observation that N_{p1} increases with the silica coating thickness from F1 to F3.

To fit the scattering data in the case of an applied field, we calculate the scattering intensities $I(\phi)$ with eq 1 for $0 \leq \phi < 2\pi$ and a fixed q-value as shown in Figure 5. Both, the scattering data and the calculated values are normalized by the corresponding average $\langle I(q)\rangle_\phi$. We keep the parameters obtained by fitting the isotropic scattering patterns (without field) that are listed in Table 1 and use ε as the only fitting parameter. The quality of the fit is substantially increased by introducing a polydispersity of the magnetic moment such that $\varepsilon \propto b_c^2$ with mean value $\bar{\varepsilon}$. The square-law is consistent with the Néel model, where the magnetization of an antiferromagnetic nanoparticle scales with the particle surface.[7] It is also informative to plot the scattering curves $I(q)$ obtained from azimuthal sector averages with width $\Delta\phi = 10°$ perpendicular and parallel to the applied magnetic field, as shown in Figure 6. When fitting these curves with the same model, we find very similar best fit values for $\bar{\varepsilon}$ (±5%), which corroborates the quality of the form factor model. The best fit values $\bar{\varepsilon}$ (according to the first fitting method) are plotted against the magnetic field in Figure 7. For sample F0, a linear dependence $\bar{\varepsilon} \propto B$ is found. An estimation of the magnetic moment of F0 particles, $\mu = 1.4 \times 10^{-19}$ J/T, is obtained from the line fitting of the F0 data, which is given by $\varepsilon(B) = (35\ T^{-1})B$. The silica coated samples F1 to F3 show a distinct deviation from a linear dependency around $B = 100$ mT. The fit yields an exponent clearly below 1 for the silica-coated samples, which signifies that their effective magnetic moments appear to decrease with increasing field strength. This is reminiscent to observations on dispersed Goethite rods,[19] where the field dependency of the effective magnetic moment is explained by a competition of the remanent moment of the rods and a negative anisotropy of their susceptibility. However, in the case of hematite the susceptibility is found to be approximately isotropic.[18] In order to investigate this behavior, we performed magnetometry on the same samples.

We measured the magnetic moment of particles of batch F0 and F2 dispersed in water on a vibrating magnetometer. In contrast to the scattering experiment, where the mean orientation of $\vec{a}$ is found, magnetometry measures the mean orientation of $\vec{\mu}$. The measured magnetization M is described with a Langevin law $M(\varepsilon) = M_{sat}L(\varepsilon) + B\chi_m$, where $L(\varepsilon) = \coth(\varepsilon) - 1/\varepsilon$ and $\varepsilon = \mu B/k_B T$. The Langevin function describes the ensemble average of noninteracting magnetic moments in thermal equilibrium, as it the case for superparamagnetic domains or dispersed, noninteracting particles. The term linear in B includes several contributions to the high field susceptibility χ_m into account: mainly the antiferromagnetic susceptibility expected for single domain hematite, but may also include finite size effects such as uncompensated spins.[20] The saturation magnetization M_{sat} (i.e., the moment remaining after removal of the high-field susceptibility), the magnetic moment μ of a single particle and the susceptibility χ_m listed in Table 1 are obtained by fitting $M(\varepsilon)$ to the experimental data shown in Figure 8. In the case of F0, we find $\mu = 1.6 \times 10^{-19}$ J/T, which is in good agreement with the value obtained from fitting the scattering patterns ($\mu = 1.4 \times 10^{-19}$ J/T). For F2 the found value of 2.8×10^{-19} J/T is considerably higher than expected from the scattering experiments.

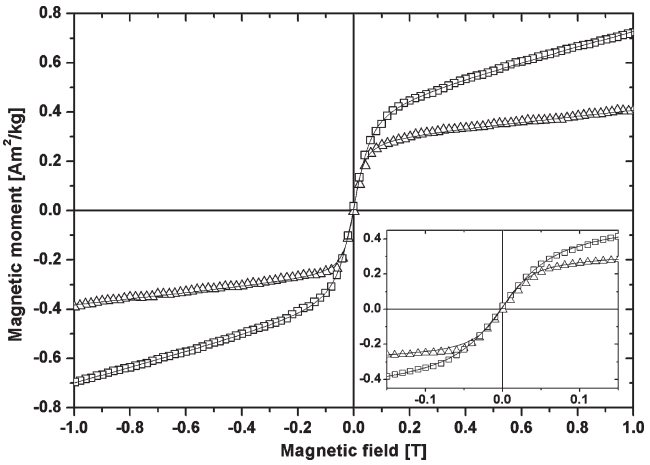

Figure 8. The magnetic moment of dispersed particles of batch F0 (squares) and F2 (triangles). Values are normalized by the amount of hematite. The lines show fits with the Langevin function described in the text. In the inset a blow-up of the low field region is shown.

In the next step we compare the orientational order of the magnetic moments $\vec{\mu}$, obtained from the magnetization curves $M(\varepsilon)$, with the orientational order of the particles $\vec{a}$ found in the scattering experiments. For a magnetic moment $\vec{\mu}$ restricted to the plane perpendicular to $\vec{a}$, we expect a strong correlation between the orientational behavior of the two vectors. The scattering experiments reveal the particle orientation and an appropriate measure for the orientational order is therefore $\cos(\xi)^2 = \sin(\phi_1)^2 \sin(\phi_3)^2$, where ξ is the angle between $\vec{a}$ and $\vec{B}$ (see Figure 1b). The associated orientational order parameter $S_2^{\vec{a}}$ is defined as

$$S_2^{\vec{a}} = \left\langle P_2\left(\frac{\vec{a}}{a} \cdot \frac{\vec{B}}{B}\right)\right\rangle = \frac{1}{Z}\int_0^{2\pi}\int_0^{\pi} p(E_{\text{pot}})P_2(\cos(\xi))\sin(\phi_3)d\phi_1 d\phi_3 \tag{4}$$

where $P_2(\cos(\xi)) = (3\cos(\xi)^2 - 1)/2$ is the second-order Legendre polynomial. It can easily be shown that $S_2^{\vec{a}} = 0$ for a randomly oriented sample, and $S_2^{\vec{a}} = -0.5$ for a fully aligned sample (i.e., $\vec{a} \perp \vec{B}$). In contrast, the Langevin function $L(\varepsilon)$ follows the first orientational order parameter $S_1^{\vec{\mu}} = \langle(\vec{\mu}/\mu)\cdot(\vec{B}/B)\rangle$, which describes the orientational order of the magnetic moments $\vec{\mu}$ in the equilibrium.[21] In this case, a fully aligned sample corresponds to $S_1^{\vec{\mu}} = 1$. As suggested by torque measurements on similar particles,[16] we assume the high-field susceptibility χ_m is of isotropic nature and does not contribute to an alignment of the particles. Therefore we subtract it from the magnetization data $M(B)$ and obtain

$$S_1^{\vec{\mu}} = \frac{M(B) - B\chi_m}{M_{\text{sat}}} \tag{5}$$

Figure 9 compares $S_2^{\vec{a}}$ obtained from the scattering data (computed with eq 4) with $S_1^{\vec{\mu}}$. The silica-coated particles (F1−F3) show a different orientational behavior in an applied magnetic field than the uncoated sample F0. As shown by the $S_2^{\vec{a}}$ data, the silica-coated particles do not align as easily as the uncoated F0 particles. In contrast, the $S_1^{\vec{\mu}}$ data shows that the magnetic moments of the silica-coated particles align better than those of the F0 particles. At a magnetic field of about 0.3 T, the silica-coated particles have $S_1^{\vec{\mu}} \simeq 1$, suggesting that the magnetic moments are fully aligned, but $S_2^{\vec{a}}$ confirms only moderate particle alignment. Such a decoupling of the magnetic moment from the particle orientation is expected for superparamagnetic relaxation, which means that the thermal energy is sufficient to trigger a spin−flip transition. It has been shown on similar particles[16] that silica coating induces superparamagnetic relaxation near room temperature. We therefore assume that, for the silica-coated particles, the superparamagnetic relaxation time (or Néel relaxation time) τ_N is on the order of the Brownian relaxation time τ_B ($\tau_B = 4\bar{a}\bar{b}^2\eta\pi/k_BT \sim 1$ ms for F2), which results in a partial decoupling of $\vec{\mu}$ and $\vec{a}$. When measured with magnetometry, the superparamagnetic relaxation allows a stronger response at low field compared to the uncoated particles that only show Brownian relaxation, which explains the larger value of μ for F2 compared to F0 (see Table 1). In contrast, the orientational order is lower for the silica-coated particles, since the particles are allowed to relax via superparamagnetic relaxation. Moreover, the more pronounced effect at high fields in Figure 7 can be understood when considering that

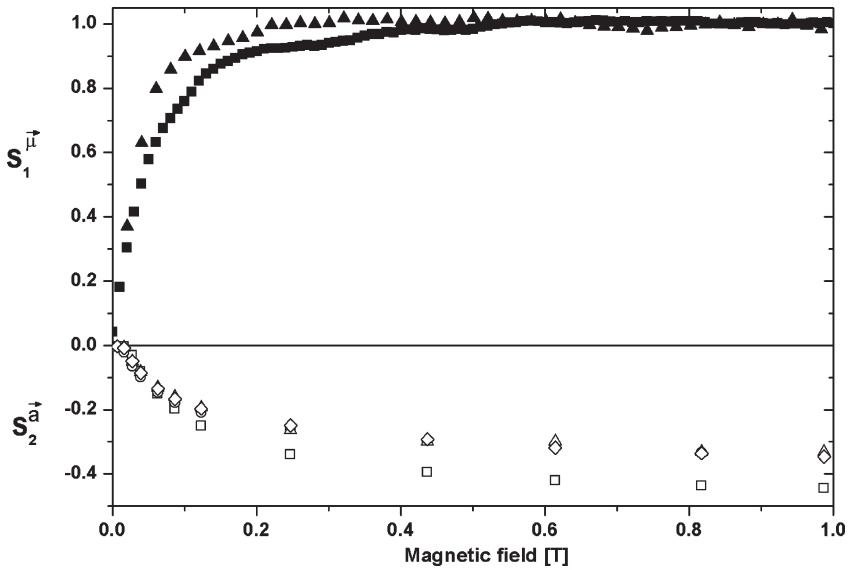

Figure 9. Orientational order parameters found from fits of the scattering curves (open symbols) and from magnetometry (filled symbols) for F0 (squares), F1 (circles), F2 (triangles) and F3 (diamonds). The silica-coated particles F1, F2, and F3 align less (based on scattering data) but their magnetic moments (based on the magnetometry data) align more compared to the uncoated particles F0.

τ_N decreases monotonically with the magnetic field.[22] These results indicate partial superparamagnetic behavior of the silica-coated particles at room temperature, which is enhanced at high fields, whereas the uncoated particles behave as weakly ferromagnetic particles.

Conclusions

It has been possible to determine the particle dimensions and silica coating thickness by SAXS measurements and applying core−shell model for the form factor. Compared to the usual characterization with a statistical analysis of TEM-images, the scattering experiments give more accurate information due to the considerably larger number of probed particles. Moreover, it provides access on the internal structure of the particles and on the porosity. The high porosity of the characterized particles is key to a better understanding of their magnetic properties and offers considerable potential for applications, e.g., as a catalyst. Furthermore, the applied model offers the possibility to track the orientational behavior of the dispersed particles. This information is important for the characterization of colloidal model systems, which might contribute to a better understanding of the phase behavior of particles with anisotropic interaction potential.

The comparison of orientational order parameters for particles with and without silica coating reveals that a silica layer substantially changes the magnetic properties of the particles. The orientational order obtained from magnetization measurements on dispersed particles allows us to elucidate on the different behavior of coated and uncoated particles in more detail. While uncoated particles display strong correlation between the direction of the magnetic moment $\vec{\mu}$ and the particle orientation $\vec{a}$, there is decoupling of $\vec{\mu}$ and $\vec{a}$ orientation for the silica-coated particles, which becomes more pronounced at high field strength. The magnetic moment, confined to the basal plane, aligns with the external field. This behavior can be attributed to superparamagnetic relaxation and is in perfect agreement with a previous study.[16] The superparamagnetic relaxation at room temperature for the silica-coated particles is unexpected, since it is normally observed for particles with diameter <30 nm only.[23] The investigated particles have formed by aggregation of subunits with a typical size of 10 nm, as suggested by Ocaña et al.[9] This indicates that these subunits set the length scale relevant for the magnetic properties and, in particular, for the superparamagnetic relaxation. If the exchange coupling between the subunits is only weak, as suggested by Mansilla et al.,[17] the mechanical stress or chemical modifications caused by the silica coating may significantly change the interaction strength so that some subunits become decoupled. This will lead to magnetic regions within the spindle that are small enough to show superparamagnetic relaxation.

This finding underlines the importance of particle morphology for the magnetic properties of porous particles and explains the wide range of magnetic properties that have been reported for such particles in the literature. The superparamagnetic character of particles of this size is also of interest for applications. The increased colloidal stability compared to particles with permanent magnetic moment, where dipole interaction can lead to aggregation, makes superparamagnetic particles promising candidates for, e.g., protein or cell separation techniques.

Acknowledgment. This work is supported by the Swiss National Science Foundation and the Adolphe Merkle Foundation. The authors also thank Camille Dagallier for TEM assistance and Malik Vivek Kumar for help with initial magnetization measurements. Further we thank Christian Moitzi for important and fruitful discussions.

References and Notes

(1) Shukoor, M. I.; Natalio, F.; Tahir, M. N.; Ksenofontov, V.; Therese, H. A.; Theato, P.; Schröder, H. C.; Müller, W. E. G.; Temel, W. *Chem. Commun.* **2007**, 4677–4679.
(2) Liu, L. H.; Dietsch, H.; Schurtenberger, P.; Yan, M. *Bioconjug. Chem.* **2009**, *20* (7), 1349–1355.
(3) Hilger, I.; Hergt, R.; Kaiser, W. A. *J. Magn. Mag. Mater.* **2005**, *293*, 314–319.
(4) Lindner, P.; Zemb, T. *Neutrons, X-rays and Light: Scattering Methods Applied to Soft Matter*; Elsevier: Amsterdam, 2002.
(5) Behler, C.; Caruthers, J.; Franses, E. *J. Chem. Phys.* **1990**, *92*, 140–156.
(6) Frenkel, D.; Mulder, B. M.; McTague, J. P. *Phys. Rev. Lett.* **1984**, *52*, 287–290.
(7) Morup, S.; Madsen, D. E.; Frandsen, C.; Bahl, C. R. H.; Hansen, M. F. *J. Phys.: Condens. Matter* **2007**, *19*, 213202.
(8) Ozaki, M.; Kratohvil, S.; Matijević, E. *J. Colloid Interface Sci.* **1984**, *102* (1), 146–151.
(9) Ocaña, M.; Morales, M. P.; Serna, C. J. *J. Colloid Interface Sci.* **1999**, *212*, 317–323.
(10) Sacanna, S.; Rossi, L.; Kuipers, B.; Philipse, A. *Langmuir* **2006**, *22*, 1822–1827.
(11) Graf, C.; Vossen, D. L.; Imhof, A.; Blaaderen, A. *Langmuir* **2003**, *19*, 6693–6700.
(12) Behler, C.; Caruthers, J.; Franses, E. *J. Chem. Phys.* **1993**, *98*, 3600–3611.
(13) Rufier, C.; Reufer, M.; Dietsch H.; Schurtenberger, P. To be submitted for publication.
(14) Sacanna, S.; Rossi, L.; Wouterse, A.; Philipse, A. P. *J. Phys.: Condens. Matter* **2007**, *19*, 376108.
(15) Suber, L.; Fiorani, D.; Imperatori, P.; Foglia, S.; Montone, A.; Zysler, R. *Nanostruct. Mat.* **1999**, *11*, 797–803.
(16) Reufer, M.; Dietsch H.; Gasser, U.; Grobety, B.; Hirt, A.; Malik, V. K.; Schurtenberger, P. To be submitted for publication.
(17) Mansilla, M.; Zysler, R.; Fiorani, D.; Suber, L. *Physica B* **2002**, *320*, 206–209.
(18) Morrish, A. H. *Canted Antiferromagnetism: Hematite*; World Scientific: Singapore, 1994.
(19) Lemaire, B. J.; Davidson, P.; Ferré, J.; Jamet, J. P.; Panine, P.; Dozov, I.; Jolivet, J. P. *Phys. Rev. Lett.* **2002**, *88*, 125507.
(20) Madsen, D. E.; Morup, S. *Phys. Rev. B* **2006**, *74*, 014405.
(21) Ilg, P.; Kröger, M.; Hess, S. *J. Chem. Phys.* **2002**, *20* (116), 9078–9088.
(22) El-Hilo, M.; O'Grady, K.; Chantrell, R. W. *J. Magn. Magn. Mater.* **1991**, *114*, 307–131.
(23) Dunlop, D. J. Özdemir, Ö. *Rock Magnetism: Fundamentals and Frontiers*; Cambridge University Press: Cambridge, 1997.